

Real-Time In-Situ Optical Tracking of Oxygen Vacancy Migration in Memristors

Giuliana Di Martino^{1,3*†}, Angela Demetriadou^{2†}, Weiwei Li^{3†}, Dean Kos¹, Bonan Zhu³, Xuejing Wang⁴, Bart de Nijs¹, Haiyan Wang⁴, Judith MacManus-Driscoll³, Jeremy Baumberg¹

¹NanoPhotonics Centre, Cavendish Laboratory, University of Cambridge, CB3 0HE, UK

²School of Physics and Astronomy, University of Birmingham, B15 2TT, UK

³Department of Materials Science and Metallurgy, University of Cambridge, CB3 0FS, UK

⁴School of Materials Engineering, Purdue University, IN 47907-2045, USA

Abstract

Resistive switches, which are also known as memristors, are low-power, nanosecond response devices that are used in a range of memory-centric technologies. Driven by an externally applied potential, the switching mechanism of valence change resistive memories involves the migration, accumulation and rearrangement of oxygen vacancies within a dielectric medium, leading to a change in electrical conductivity. The ability to look inside these devices and understand how morphological changes characterise their function has been vital in their development. However, current technologies are often destructive and invasive. Here, we report a non-destructive optical spectroscopy technique that can detect the motion of a few hundred oxygen vacancies with nanometre-scale sensitivity. Resistive switches are arranged in a nanoparticle-on-mirror geometry to exploit the high optical sensitivity to morphological changes occurring in tightly confined plasmonic hotspots within the switching material. Using the approach, we find that nanoscale oxygen bubbles form at the surface of a strontium titanate memristor film leading ultimately to device breakdown on cycling.

Main

Resistive random-access memories (RRAMs) are promising emerging devices for logic-in-memory operations due to their high-density integration and scalability, ultra-fast access times, low power consumption and ease of fabrication¹. RRAMs can be classified as conductive bridge random access memories (CBRAM, also called electrochemical metallization cells) or redox random access memories (ReRAM, also called valence change mechanism cells)^{2,3}. In CBRAM cells, a nanoscale conductive metallic path between a working electrode/anode (often electrochemically active, such as silver or copper) and a counter electrode/cathode

(often inert, such as platinum, gold or titanium nitride) is formed or broken by generation, movement and reduction of mobile metal cations (i.e. Ag^+ or Cu^{2+} , for example)⁴. ReRAMs occur in a wide range of transition metal oxides^{5,6} and are typically triggered by migration of anions such as oxygen (usually described by the motion of the corresponding oxygen vacancies). The subsequent modified stoichiometry leads to redox reactions from valence changes of the cation sublattice and changes in the electronic conductivity at the electrode interface^{7–10}. Sometimes, ions can oxidise upon reaching the positive electrode via the half-reaction $2\text{O}^{2-} \rightarrow 4e^- + \text{O}_{2(\text{g})}$, forming bubbles of oxygen gas¹¹. With such ReRAM devices, it is important to identify and understand the failure mechanisms that impact endurance and variations in memristive device parameters, thus avoiding the extra energy required to eliminate the impact of process variations, which modify geometries, thicknesses and contact areas^{6,12,13}).

Widely used characterization methods – such as voltage-sweep and voltage-pulse measurements, electrochemical cyclic voltammetry, and *ex-situ* and *in-situ* electron microscopy – do not provide a full description of the switching dynamics in either CBRAM or ReRAM. Slow device switching in voltage-sweep measurements leads to artifacts in the switching behavior¹⁴. Pulse measurements do not characterize the full voltage-current behavior of the device^{15,16}, whereas cyclic voltammetry does not distinguish the very localized resistive switching effects with little insight into the morphology and geometry of the formed filaments¹⁷. *Ex situ* transmission electron microscopy (TEM) allows for high-resolution imaging of filaments and metal clusters, as well as the modified morphology of the switching material but only before and after switching^{18–20}.

In ReRAMs, the use of TEM can be challenging due to low image contrast between oxygen-rich and deficient regions. Nevertheless, some studies have imaged conductive phases in ReRAM cells. The formation and rupture of a sub-stoichiometric and conductive Magnéli phase in TiO_2 with a diameter as low as 10 nm has, for instance, been demonstrated²¹. Additionally, *in-situ* TEM operation conditions and samples differ from resistive switches in practical applications. Devices are typically prepared on electron-transparent silicon nitride windows and the electrons used for imaging can perturb the drift of the charged ions.

Large optical field enhancements in nanoplasmonic systems have proven to be useful in understanding the dynamics involved in the switching processes in CBRAM devices^{22–24}. New information can be obtained without perturbing the system by creating optically-accessible CBRAM switches and monitoring in real-time the scattering signal coming from the plasmonic field tightly confined to the nanometre-scale switching gap. The optical spectrum of the

plasmonic hotspot in the junction shows the creation and destruction of conductive channels between the electrodes, tracking morphological changes occurring in the switching material. In this Article, we adopt this technique in order to observe the valence change mechanism in ReRAM devices. In particular, we examine the motion of oxygen vacancies within the switching material strontium titanate (SrTiO₃), which is otherwise invisible to non-invasive electron microscopy techniques.

Device structure and experimental setup

We fabricate cells with a conventional TiN/ SrTiO₃ (TiN/STO) layer stack and a Au-nanoparticle (NP) top electrode (Fig. 1a, b). The STO acts as switching material, while the bottom conducting TiN layer forms the counter-electrode. Since widely adopted for ReRAM cells^{25–27}, STO is an ideal model material system. We emphasise that the optical properties of TiN follow a Drude-like behaviour, similar to Au, thus forming nanogaps with strong plasmonic field confinement when close to metallic nanoparticles (nanoparticle-on-mirror geometry²⁸, Fig. 1a).

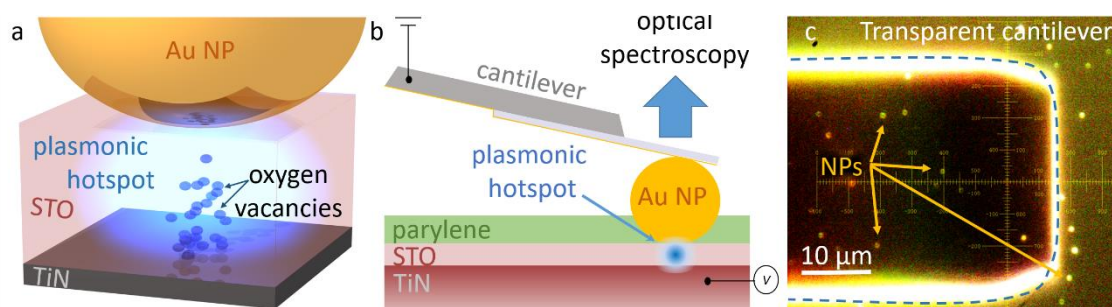


Figure 1 | Memristive device in a plasmonic geometry. **a**, ReRAM in a nanoparticle-on-mirror (NPoM) geometry, with plasmonic field tightly confined in the spacer material STO between a Au nanoparticle (NP) and TiN film. **b**, Optical spectroscopy is performed through a transparent but electrically conductive cantilever used to contact each individual AuNP isolated by the surrounding insulating parylene layer. **c**, Dark field top view of AuNPs on STO layer seen through the cantilever.

The nanoparticles-on-mirror (NPoM) are individually electrically contacted from the top using a flexible transparent Si₃N₄ tip-less cantilever coated with 3 nm Cr and 6 nm Au, yielding $\sim 3 \Omega/\square$ resistance (Fig. 1b). This allows unobstructed observation of the AuNP scattering under the cantilever through dark field spectroscopy (Fig. 1b,c). The density of AuNPs (80 nm diameter) on the sample surface is further reduced in the deposition phase to ensure NPoM structures are individually contacted, with the large cantilever area ensuring edge scattering is not collected. Compared to highly-scattering AFM tips, this cantilever contacting allows optical access to the very inner regions of the device. To further ensure electrical connection

only through the AuNP without any direct cantilever contact with the STO surface, the system is conformally coated with an insulating parylene layer, which is then dry etched to expose the AuNP crown while maintaining a pinhole-free insulating barrier over the surrounding surface (Methods).

The valence change mechanism is responsible for the switching process in this cell with the oxygen vacancies experiencing drift under bias through the STO layer. Resistive switching is enabled by a voltage (typically 8 V – 12 V) applied to the TiN. We use $<10 \mu\text{A}$ current compliance to restrict the maximum current in the low resistive ON state (LRS).

In our measurements, the cantilever is gradually lowered into contact with the top of an isolated NPoM structure until it is locally parallel to the device top surface. Cantilever position and tilt orientation are controlled within $<1 \text{ nm}$ and $<0.2^\circ$ using a piezoelectric stage and observing the wedged interference fringes created by the cantilever when approaching the Au mirror. Compared to the $>10 \text{ GPa}$ Van der Waals forces across these nm metal gaps, the cantilever makes little difference ($\sim 0.04 \text{ GPa}$) because it accommodates contact by bending along its $200 \mu\text{m}$ length (see Methods). The pressures used here are within a safe range where they play no role in the switching (see Supplementary Information, section G)²⁹.

We record the dark-field scattering spectra and voltage-current signals simultaneously. The localized plasmons of each AuNP couple to their image charges in the TiN film underneath the STO spacer layer forming a confined plasmonic hotspot, similar to a nanoparticle dimer^{30,31}. The NPoM configuration has been extensively investigated²⁸. The optical response of this system is measured by illuminating the sample with a white light beam incident at 60° and collecting the scattered light through a dark-field objective (Methods). Light is collected by a cooled spectrometer and CCD camera.

Experimental optical investigation of switching cycles

We focus our attention on two sets of samples with STO thicknesses $d = 8 \text{ nm}$ (named D_8 , Fig. 2a-c) and 4 nm (named D_4 , Fig. 2d-i) respectively, as demonstrated via cross-sectional transmission electron microscopy (see Supporting Information Fig. S4). The results are representative but the behavior for each specific cell slightly differs in detail - spectral changes are consistently observed only upon switching, but the change of intensity or peak position can vary due to the nature of the switching mechanism (Supporting Information Fig. S1), involving stochastic processes and a complex interplay between electrochemical and diffusion effects (Supporting Information, section H). The cells here switch to the LRS at a SET voltage V_{SET} , defined as the voltage where the current abruptly changes from $<40 \text{ pA}$ to

several nA (Fig. 2b) or μA (Fig. 2f). Applying a negative voltage results in a RESET of the cell (switching back to the high resistance OFF state, HRS).

For D_8 , the AuNP scattering spectra show a strong plasmon resonance at $\lambda_1 \sim 610$ nm (Fig. 2a, c - I). Focusing on times preceding the clear electrical switching event ($20\text{s} < t < 30\text{s}$), the longer wavelength peak $\lambda_2 \sim 780$ nm grows (Fig. 2a, c - II). After the SET event happens at $\sim 30\text{s}$, the total conductance reaches $10^{-5} G_0$ ($30\text{s} < t < 70\text{s}$), well below that for an atomic point contact ($G_0 = 77.5\mu\text{S}$ is the quantum conductance), as expected for ReRAM systems with narrow conductive filaments³². In fact, the presence of oxygen vacancy paths in the dielectric gives extended bands in the gap³³, resulting in conductance $G \sim G_0$ for one vacancy path³⁴ and $G \ll G_0$ when several vacancies are removed from the single-vacancy filament, hence positioning the energy of the first subband just above the electrode Fermi level³². While for this device the peak scattering λ_1 changes little with time, its intensity transiently halves following the switching event (Fig. 2a, c - III). In contrast, the longer wavelength peak λ_2 retains its intensity with only a few nm redshift. After the RESET event ($t > 70\text{s}$), the λ_1 peak intensity increases to its value before switching while the λ_2 peak remains (Fig. 2a, c - IV). This highlights the non-reversibility of the ReRAM switching process which is unable²⁵ to bring the system back to the morphology of a pristine cell (I). Only 3 switching cycles are observed for D_8 .

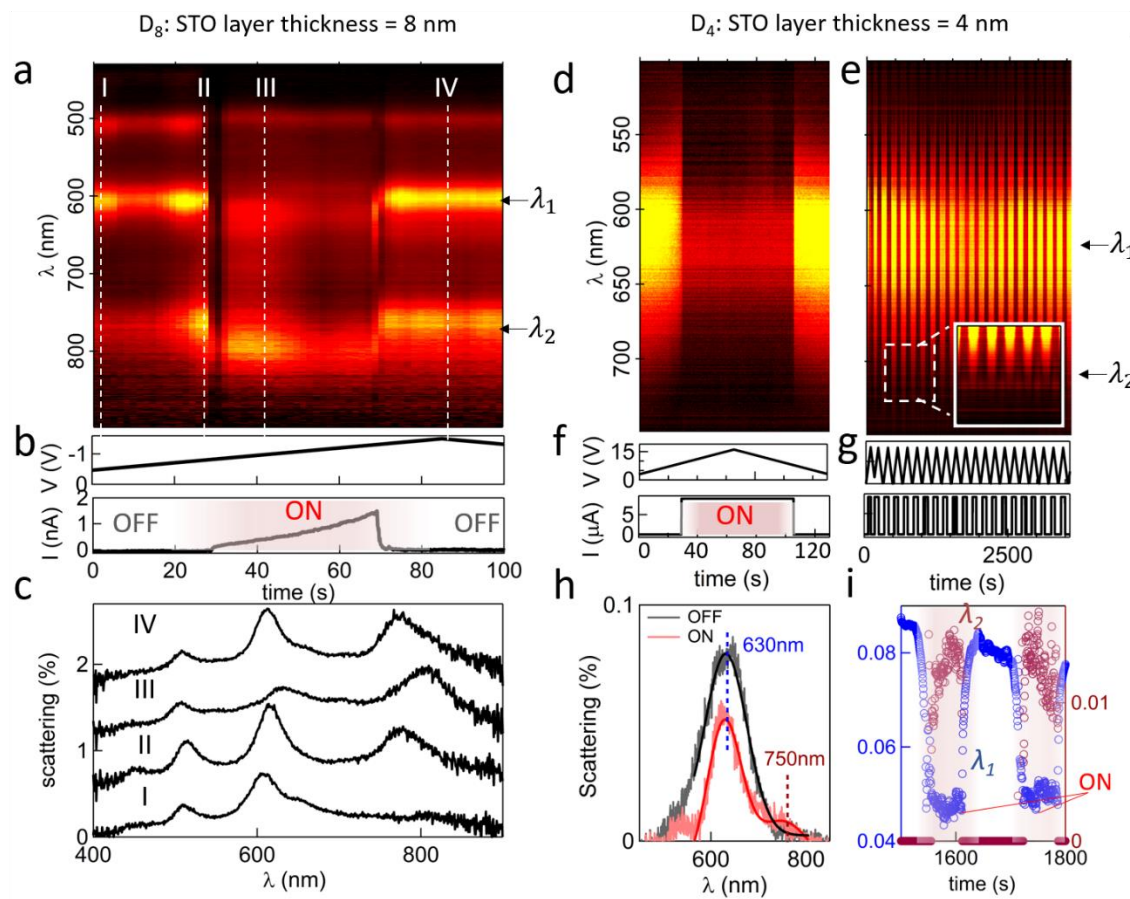


Figure 2 | Switching cycles of NPoM memristive cell. **a**, Scattering intensity collected simultaneously with **b**, the electrical signal (voltage and current) from a single AuNP on D_8 . Dashed lines show times highlighted in **c**, giving spectra for (I) pristine sample, (II) device pre-switching, (III) device switched ON and (IV) reset of device into OFF state. A clear peak appears in the infrared ($\lambda_2 \sim 780\text{-}800$ nm) without disappearing upon RESET. **d-e**, Scattering intensity collected simultaneously with **f-g**, the electrical signal (voltage and current) from a single AuNP on D_4 . Weaker scatter is observed with a strong $\lambda_1 \sim 630$ nm peak and a weak $\lambda_2 \sim 750$ nm peak (highlighted as inset in **d**). **h**, Detailed ON (red) and OFF (black) spectra with multi-peak fits and **i**, extracted $\lambda_1 \sim 630$ nm (blue) and $\lambda_2 \sim 750$ nm (purple) intensity oscillations with switching (ON, shaded).

Turning our attention to D_4 (Fig. 2d-i), we observe switching over multiple cycles when the applied voltage is repeatedly switched (Fig. 2e,g). Again a shorter wavelength mode $\lambda_1 \sim 630$ nm is identified, with an intensity which reduces upon switching, as in D_8 (Fig. 2d,h,i). A longer wavelength peak $\lambda_2 \sim 750$ nm is again visible upon switching (Fig. 2h, red) but, in contrast with D_8 , it is much weaker and completely disappears upon RESET (Fig. 2i, purple). D_4 thus shows fully reversible switching, highlighting how this system can return to the morphology of a pristine cell. While switching events here progress over tens of seconds, faster voltage sweeps result in faster switching.

To confirm that the measured optical signatures arise from the bias-induced drift of oxygen vacancies within the STO layer, we study samples where the oxygen vacancies are

substantially removed by annealing (cooled in 40 kPa O₂ after film growth). No switching events are measured and a completely constant scattering signal is observed even when voltage is applied (Supporting Information Figure Fig. S2).

Tracking oxygen vacancies drift and nano-bubbles formation

To link the optical signatures observed experimentally with the various morphology regimes, we use a combination of Density Functional Theory (DFT) calculations and Finite-Difference Time-Domain (FDTD) simulations (Methods) to meticulously analyse how oxygen vacancy drift influences the plasmonic modes in the STO layers, and therefore the spectra measured experimentally.

In the NPoM structure, aligning the lower NP facet (typically $w = 20\text{--}30$ nm wide) against the flat mirror (Fig. 3c,d) creates a thin plasmonic cavity that supports multiple ‘cavity’ resonances or gap modes³⁵. Plasmon oscillations in the nanoparticle perpendicular to the surface induce image charges within the TiN mirror, confining the field within the gap, and giving rise to the plasmon cavity modes studied extensively elsewhere^{36–38}. The plasmon cavity modes appear at specific energies depending on the mirror (TiN) and nanoparticle (Au) materials as well as the presence of a TiO₂ layer, confirmed by TEM (Supporting Information, Fig.S4), resulting from the oxidation of the top few nm of TiN during STO growth (Fig. 3c,d). Figure 3b shows the field enhancement in the middle of the STO layer, where the energetically lowest mode appearing at $\sim 760\text{--}790$ nm (depending on the STO thickness) is a dark mode l_{11} . The first bright mode appears at ~ 680 nm for both devices, which is commonly referred to as the ‘dipole’ mode or l_{10} . The quadrupole resonance l_{20} appears at ~ 550 nm for both devices. The scattering cross-sections/radiative spectra of the two devices are shown in Figure 2e-h, where only the l_{10} mode radiates significantly, while the l_{11} mode absorbs producing a dip in the radiative spectra. Hence, the scattering peak measured at longer wavelengths > 800 nm, is not in fact a resonance of the system, but the result of the superposition of the dark mode l_{11} on the broad tail of the bright mode l_{10} . Our experiments show narrower resonances, probably due to weaker absorption in the measured system than expected from literature dielectric constants^{39,40}, but the resonances are fairly consistent between the experiment and simulation.

The oxygen vacancy bridge formed between the nanoparticle and the TiN mirror allows current to flow between the two structures, once a bias is applied. The optical properties of

STO change when it fills with oxygen vacancies. To calculate this, we use DFT considering a 2x2x2 supercell with 24 oxygens to simulate SrTiO_{3-δ}. From the energy levels, we obtain the corresponding dielectric functions, with vacancy concentrations from $\alpha = 4\%$ to 20% (1/24 to 5/24), see Supporting Information Figure S5.

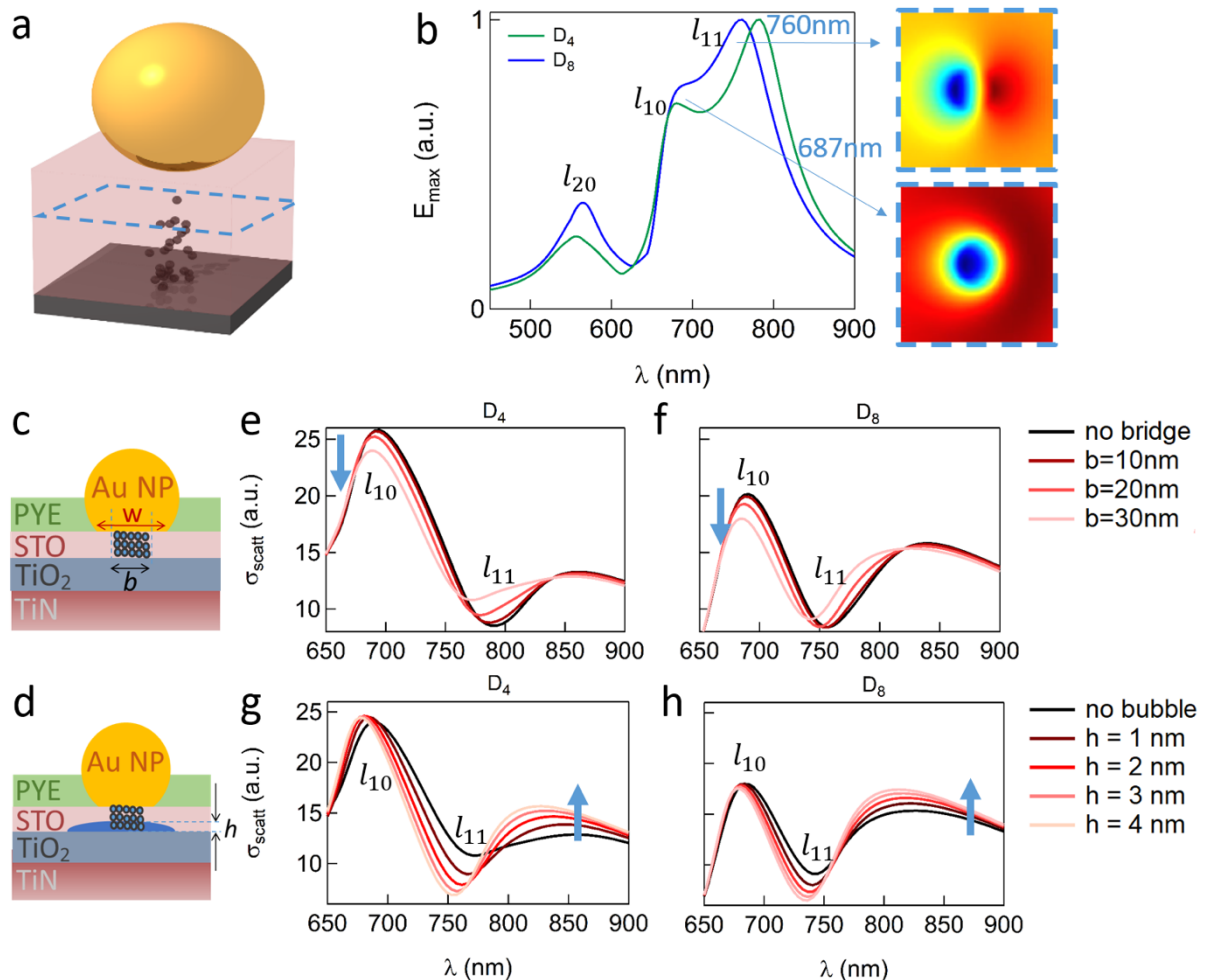


Figure 3 | Numerical simulation of optical gap modes. **a**, Geometry of NP above oxygen vacancy accumulation region, field cuts taken over mid-gap blue dashed plane parallel to substrate. **b**, First order bright and dark modes l_{10} and l_{11} at 687 nm and 760 nm and second order mode l_{20} at 550 nm, respectively **c**, NPoM with oxygen vacancy-rich bridge linking AuNP (facet $w = 30$ nm) to surface and **d**, with O₂ bubble formation. Corresponding finite-difference time domain simulation modes for the two STO thicknesses varying **e,f**, bridge width $b = 0, 10, 20, 30$ nm and **g,h**, oxygen bubble height $h = 0, 1, 2, 3, 4$ nm after bridge of $b = 30$ nm is formed.

To parametrize the influence of oxygen-vacancy-rich bridges on the spectral far-field response of the NPoM system, we incorporate these DFT optical properties into FDTD simulations of the bridge between TiN and 80 nm AuNP with fixed circular facet diameter $w = 30$ nm (Fig. 3c). This is progressively conductively connected to the Au surface through a bridge with a

content of 4% oxygen vacancies in the center of the NP facet. The diameter of the cylindrical conductive bridge is varied from $b = 0$ to 30 nm from no connection, to a bridge with a size that equals the full facet, giving optical spectra shown in Figure 3e,f. The l_{10} resonance blue-shifts and its scattering amplitude decreases by up to $\sim 30\%$ as the vacancy bridge is formed. This corresponds well with experiment (Fig. 2 a,d) where the scattering of both devices decreases at 600 nm when current flows between the nanoparticle and the TiN mirror (i.e. the device is ON), though the peak positions are slightly shifted. While the behaviour is qualitatively predicted, the intensity change ($\sim 150\%$ for experiments in D₄, Supporting Information Fig. S14) might be influenced by slight variations of refractive index from the DFT predictions.

By contrast, the peak at 840nm is barely affected by the conductive vacancy bridge, indicating that an additional process, more dominant for D₈, occurs. To explain the observed spectral shifts we are forced to conclude that with enough oxygen vacancies, the dense oxygen at the other electrode reversibly converts to O₂ gas, strongly perturbing the scattering response. As previously found, ultrathin oxide layers can reversibly form oxygen under high fields⁴¹. To study the influence of O₂ content on the spectral far-field response, FDTD simulations are performed with a fixed facet diameter $w = 30$ nm, fixed bridge size $b = 30$ nm and thin dome-shaped oxygen bubble height at the STO interface varied from $h=0-4$ nm (Fig. 3g,h). These scattering spectra show the O₂ reservoir has a very strong impact on the scattering strength ~ 840 nm, but negligible change to the l_{10} mode scattering peak at ~ 700 nm. Note that for D₈, the scattering intensity at 840 nm is substantially brighter for larger O₂ reservoirs and reaches similar values to the l_{10} mode scattering at ~ 700 nm. This behaviour is in agreement with the experimental results of Figure 2a-c, where the $\lambda_2 \sim 800$ nm peak has stronger scattering intensity.

From our simulations, we thus conclude that changes to the main bright l_{10} mode at $\lambda_1 \sim 600$ nm are due to the formation of the current-carrying vacancy bridge, which eventually turns the device ON, while changes to the $\lambda_2 \sim 800$ nm peak come from superposed l_{10} and l_{11} modes arising from formation of an O₂ nano-reservoir at the STO/TiO₂ interface⁴². Each spectral peak can be independently used as a signature for *real-time* and *in-situ* readout of morphological changes occurring in the STO switching material, with few nanometre resolution (lateral optical mode FWHM $\sqrt{wd} \sim 11$ nm and 15 nm for D₄ and D₈, respectively, see Supplementary information, Fig. S12). Changes in l_{10} scattering intensity enable us to resolve the construction of these oxygen vacancy bridges for long times before the actual SET event, even though the electrical signature only shows a sharp transition into the ON state (Supplementary information, Fig. S14c). To highlight this ability to link nanoscale

morphological changes to scattering spectra, we simulate the full evolution through a switching cycle (Fig. 4a). The pristine sample (#0) with no conductive bridge and no O₂ bubble, initially grows through (#1-2) an O₂ reservoir of height $h = 2$ nm, to a conductive bridge (ON, #3-5) of $w = 30$ nm together with an O₂ reservoir of $h = 2-4$ nm. After (RESET, #6-8) no conductive bridge remains, but an oxygen bubble of $h = 4$ nm is left behind. While our model is necessarily simplistic, it is able to reproduce the experimental switching event depicted in Figure 2a, with the corresponding spectra I,II,III,IV matching between experiment and simulations (Fig. 4) supporting our explanation. Comparing the intensity change for λ_2 peak both in experimental and simulated scattering spectra, enables us to optically track the bubble formation and its enlargement (Supporting Information, Figure Fig. S13). The $\sim 90\%$ increase in scattering intensity at λ_2 in the pre-switching phase (II) of D₈ matches our FTDT simulations of the long wavelength peak when an 8 nm O₂ bubble is formed in the STO layer. This highlights the substantial material transformation which characterizes the poor switching behaviour of D₈.

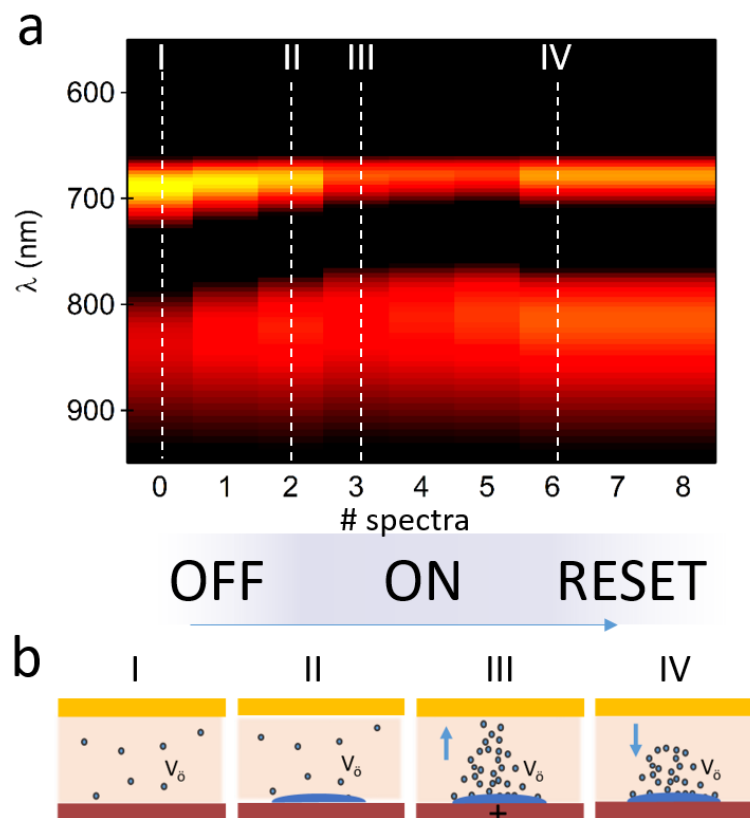


Figure 4 | Numerical simulations of optical modes through first switching cycle. a, Scattering intensities of structures shown in **b**, (I) oxygen vacancies distributed through pristine sample, (II) device pre-switching with $h = 2$ nm, (III) device switched ON with $h = 2$ nm, $b = 30$ nm, and (IV) resetting of device into OFF state with $h = 4$ nm.

The first switching event of D_8 highlights non-reversible behaviour and shows the considerable stress built into the STO. This results in non-stable devices unable to perform multiple cycles, so that early breakage is observed. By contrast, D_4 (Fig. 2d-g) is characterized by continuous repeatable switching. From its spectroscopic signature showing the plasmonic modes λ_1 consistently decreasing (oxygen vacancy accumulation) and λ_2 increasing (O_2 bubble formation) in intensity with switching over multiple cycles, we conclude that the O_2 reservoir is fully reabsorbed into the structure after every RESET event. In our study the devices with 8nm STO thickness were more prone to fail, whereas devices with 4nm STO thickness allowed for hundreds of cycles (Fig. S15,d). Optical signatures of oxygen bubbles present in the 8nm device (which possibly has a larger (thicker) STO reservoir of vacancies) suggest this plays a significant role in the failure mechanism.

Similar results are obtained for other devices and show how spectroscopy is able to characterise the movement of oxygen vacancies before any electrical transport changes can be resolved (Supporting Information, Figure Fig. S14c), as well as show that oxygen nanobubble formation at the TiN/STO interface is a key cause of failure. We underline how such optical spectroscopy finally enables the improved understanding of causes leading to device breakdown. This is achieved with an *in-situ* technique that tracks *in real time*, under ambient conditions, and without perturbing the system, oxygen vacancy migration within few nm of switching layer, that can thus be combined with other techniques and environmental conditions.

Conclusions

We have linked the fields of nanoscale device engineering and plasmon-enhanced light-matter interactions to implement optically accessible resistive switches. A conductive transparent cantilever with nanoparticle-mediated electrical contacts provides a useful and non-destructive method to characterize the resistive switching effect in ReRAM devices. Avoiding the impact of electron beams and the need for lateral junctions (required for electron beams to access the region of the filament formation) are key benefits of this approach. Our experimental and numerical investigation generates new insight into the mechanism behind drift and accumulation of oxygen vacancies, creation of a conductive channel between the electrodes, and formation of nanometre-size oxygen bubbles at the lower switching material interface. Our numerical framework couples each spectral peak to the drift of oxygen vacancies and to the formation of an O_2 reservoir at the STO/ TiO_2 interface. The change of scattering intensity of the optical mode assigned to the bridge formation enable us to resolve the drift of oxygen vacancies in the $\sim 30s$ before the SET event, showing

only a sharp transition when the ON state is reached. Our approach also helps to identify the breakdown mechanisms upon cycling. Future improvements in the technique will aim to decrease the switching voltages by reducing the dielectric spacer thickness, which has the additional benefit of trapping the light more tightly in the nanogap, thus increasing the spectroscopic signatures of filament dynamics and accessing faster timescales.

Methods

Sample preparation. Epitaxial SrTiO₃/TiN bilayer films were grown on (001)-oriented MgO substrates by pulsed laser deposition (PLD). Before growing the bilayer films, (001)-oriented MgO substrates were annealed *in-situ* at 950 °C for 2 hours in vacuum. The TiN layer (~ 40 nm) was fabricated using a substrate temperature of 650 °C in an argon partial pressure of 1 mTorr with laser fluence of 1.5 J·cm⁻². Then the substrate temperature was increased to 750 °C in an oxygen partial pressure of 1 mTorr for growing the SrTiO₃ layer. After deposition, the films were cooled to room temperature at a rate of 10 °C/min under an oxygen pressure of 1 mTorr. To further remove oxygen vacancies, some films were cooled under oxygen partial pressures of 300 Torr. The growth dynamics were investigated by real-time monitoring of the intensity variations of various features in the reflection high-energy electron diffraction (RHEED) patterns. Gold nanoparticles (AuNPs, 80 nm diameter in citrate buffer) from BBI Solutions are drop-cast on the substrate to obtain a number density of ~10⁻³ μm⁻² on the STO surface. A 350 nm layer of parylene-C (SCS Labcoter 2) is deposited on top of the entire sample, and then etched with O₂ plasma to expose the top of the AuNPs while leaving a 20 nm insulating layer around the particles. Etching is performed in steps while monitoring the parylene thickness with an ellipsometer (Woollam alpha-SE).

Sample characterization. The phase and the crystalline quality of the thin films were investigated by ω-2θ X-ray diffraction (XRD, high resolution Panalytical Empyrean vertical diffractometer, Cu Kα radiation) and high-resolution transmission electron microscopy (HRTEM, FEI FEI Talos 200X TEM). The surface morphologies were examined by atomic force microscopy (AFM). HRTEM images, selected area diffraction (SAD) patterns and EDX elemental maps (Supporting Information Figure S4) are used to estimate layer thicknesses and show the presence of TiO₂ layer between STO and TiN.

Optical setup. Plasmon resonances of AuNPs are characterized by scattering spectra and colour images. The sample is illuminated by high-angle white light incident through a 100x DF 0.8 NA objective (LMPlanFLN) in an optical dark field configuration. The same objective is used for collection of scattering spectra and images. The dark field scattered light is then sent to a CCD camera (Lumenera Infinity 2) and spectrometer (Ocean Optics QE65000) for spectral analysis. Spectral content of the scattered light was measured with 1s or 0.5s integration times (time resolution is limited by the light intensity, with brighter light sources capable of bring integration times down to 10 μs).

Electrical measurements. For electrical characterization, a Keithley 2635 Source meter is used in a 4-wire configuration with triaxial connections, which allows low-noise measurement of currents down to 10 pA. In all measurements, the Au top electrode is grounded. Voltage is ramped and a sweep rate of 0.18 V/s is used. A measurement range of 100 μ A is used to keep the integration time and sweep rate constant. All measurements are performed in air at room temperature.

Cantilever contacting. Transparent tipless SiN AFM cantilevers (AppNano) are coated with 3 nm Cr and 6nm Au by e-beam evaporation, providing a transparent conductive coating. Tips are mounted on a custom-built mount controlled by XYZR piezoelectric positioners and integrated with the microscopy setup. The cantilever spring constant is $k = 35\text{mN/m}$ (as measured during manufacture), resulting in a pressure on our gap region of 0.04GPa (see Supporting Information, Sec.G).

Numerical simulations. Density functional theory (DFT) calculations were carried out using plane wave pseudopotential code CASTEP⁴³. The optical dielectric functions were calculated by OptaDOS⁴⁴. A commercial simulator based on the finite-difference time-domain (FDTD) method was used to perform the calculations of the far-field scattering spectra and near-field distributions (Lumerical Inc⁴⁵).

Acknowledgements

GD acknowledges support from the Winton Programme for the Physics of Sustainability, J.J.B acknowledges funding from EPSRC grant EP/L027151/1, W.-W.L. and J.L.M.-D. from EPSRC grants EP/L011700/1, EP/N004272/1, EP/P007767/1 and the Isaac Newton Trust. AD acknowledges support from a Royal Society University Research Fellowship URF\R1\180097 and Royal Society Research Fellows Enhancement Award RGF\EA\181038, BdN acknowledges support from the Leverhulme Trust and the Isaac Newton Trust in the form of an ECF. The US-UK collaborative effort was funded by the U.S. National Science Foundation (ECCS-1902644 (Purdue University), ECCS-1902623 (University at Buffalo, SUNY) and the EPSRC, grant EP/T012218/1. J.D. also acknowledges funding from the UK Royal Academy of Engineering, grant CiET1819_24. B.Z. acknowledges support from China Scholarship Council and Cambridge Commonwealth, European and International Trust.

Author Contributions

†These authors contributed equally. Experiments were devised and performed by G.D., with support for the chemical nanoassembly and sample preparation from D.K. The custom made

cantilever contacting setup was realised by D.K. W.-W.L. synthesized the STO/TiN films, performed X-ray diffraction and atomic force microscopy, with support from X.W. and H.W. for the TEM measurements. DFT calculations were performed by B.Z. guided by W.-W.L. and FDTD simulations by A.D. The data analysis was performed by G.D., with support from all the authors. The manuscript was written with contributions from all authors.

Corresponding Authors

*E-mail: gd392@cam.ac.uk.

Supporting Information

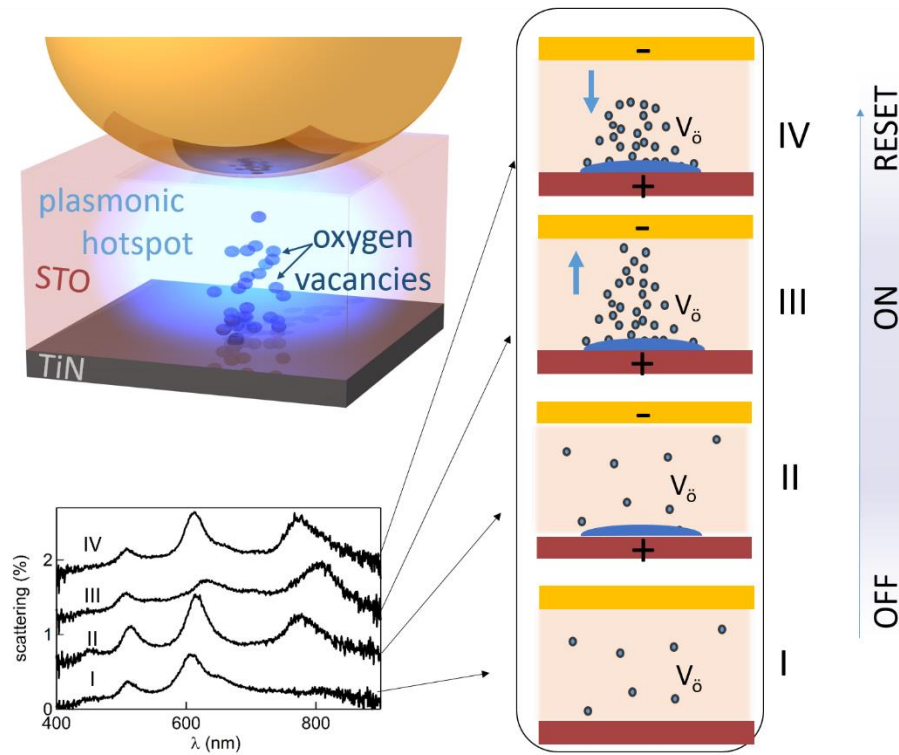
Supporting Information Available: additional spectral dynamics for as deposited and annealed samples; materials characterization of the device layers; DFT calculation for bulk and defective STO refractive index; near-field and far-field distributions of NPoM on STO layer-FDTD simulations; scattering intensity % change with O₂ bubble and vacancies bridge formation; electrical characterization of the switching process; contact force between NP and cantilever; statistical variations in current characteristics. This material is available free of charge via the Internet at <http://>.

Source data can be found at <https://doi.org/10.17863/CAM.55556>.

Notes

The authors declare no competing financial interest.

TOC



References

1. Siemon, A. *et al.* Realization of Boolean Logic Functionality Using Redox-Based Memristive Devices. *Adv. Funct. Mater.* **25**, 6414–6423 (2015).
2. Valov, I., Waser, R., Jameson, J. R. & Kozicki, M. N. Electrochemical metallization memories—fundamentals, applications, prospects. *Nanotechnology* **22**, 289502 (2011).
3. Waser, R. & Aono, M. Nanoionics-based resistive switching memories. *Nat. Mater.* **6**, 833–840 (2007).
4. Bernard, Y., Renard, V. T., Gonon, P. & Jousseume, V. Back-end-of-line compatible Conductive Bridging RAM based on Cu and SiO₂. *Microelectron. Eng.* **88**, 814–816 (2011).
5. Das, M., Kumar, A., Singh, R., Htay, M. T. & Mukherjee, S. Realization of synaptic learning and memory functions in Y₂O₃ based memristive device fabricated by dual ion beam sputtering. *Nanotechnology* **29**, 055203 (2018).

6. Niu, D., Chen, Y., Xu, C. & Xie, Y. Impact of process variations on emerging memristor. in *Proceedings of the 47th Design Automation Conference* 877–882 (Association for Computing Machinery, 2010). doi:10.1145/1837274.1837495.
7. Kwon, D.-H. *et al.* Atomic structure of conducting nanofilaments in TiO₂ resistive switching memory. *Nat. Nanotechnol.* **5**, 148–153 (2010).
8. Chen, J.-Y. *et al.* Dynamic Evolution of Conducting Nanofilament in Resistive Switching Memories. *Nano Lett.* **13**, 3671–3677 (2013).
9. Choi, B. J. *et al.* Resistive switching mechanism of TiO₂ thin films grown by atomic-layer deposition. *J. Appl. Phys.* **98**, 033715 (2005).
10. Szot, K., Speier, W., Bihlmayer, G. & Waser, R. Switching the electrical resistance of individual dislocations in single-crystalline SrTiO₃. *Nat. Mater.* **5**, 312–320 (2006).
11. Yang, J. J. *et al.* The mechanism of electroforming of metal oxide memristive switches. *Nanotechnology* **20**, 215201 (2009).
12. Das, M. *et al.* Effect of Surface Variations on the Performance of Yttria Based Memristive System. *IEEE Electron Device Lett.* **39**, 1852–1855 (2018).
13. Ahmed, T. *et al.* Inducing tunable switching behavior in a single memristor. *Appl. Mater. Today* **11**, 280–290 (2018).
14. Sun, B. *et al.* The Effect of Current Compliance on the Resistive Switching Behaviors in TiN/ZrO₂/Pt Memory Device. *Jpn. J. Appl. Phys.* **48**, 04C061 (2009).
15. Krishnan, K., Aono, M. & Tsuruoka, T. Kinetic factors determining conducting filament formation in solid polymer electrolyte based planar devices. *Nanoscale* (2016) doi:10.1039/C6NR00569A.
16. Menzel, S., Böttger, U., Wimmer, M. & Salinga, M. Physics of the Switching Kinetics in Resistive Memories. *Adv. Funct. Mater.* **25**, 6306–6325 (2015).
17. Tappertzhofen, S., Menzel, S., Valov, I. & Waser, R. Redox processes in silicon dioxide thin films using copper microelectrodes. *Appl. Phys. Lett.* **99**, 203103 (2011).

18. Hubbard, W. A. *et al.* Nanofilament Formation and Regeneration During Cu/Al₂O₃ Resistive Memory Switching. *Nano Lett.* **15**, 3983–3987 (2015).
19. D’Aquila, K., Liu, Y., Iddir, H. & Petford-Long, A. K. In situ TEM study of reversible and irreversible electroforming in Pt/Ti:NiO/Pt heterostructures. *Phys. Status Solidi RRL - Rapid Res. Lett.* **9**, 301–306 (2015).
20. Yang, Y. & Lu, W. D. Progress in the Characterizations and Understanding of Conducting Filaments in Resistive Switching Devices. *IEEE Trans. Nanotechnol.* **PP**, 1–1 (2016).
21. Kwon, D.-H. *et al.* Atomic structure of conducting nanofilaments in TiO₂ resistive switching memory. *Nat. Nanotechnol.* **5**, 148–153 (2010).
22. Di Martino, G., Tappertzhofen, S., Hofmann, S. & Baumberg, J. Nanoscale Plasmon-Enhanced Spectroscopy in Memristive Switches. *Small* **12**, 1334–1341 (2016).
23. Emboras, A. *et al.* Atomic Scale Photodetection Enabled by a Memristive Junction. *ACS Nano* **12**, 6706–6713 (2018).
24. Emboras, A. *et al.* Atomic Scale Plasmonic Switch. *Nano Lett.* **16**, 709–714 (2016).
25. Rainer Waser. *Nanoelectronics and Information Technology: Advanced Electronic Materials and Novel Devices.* (Wiley, 2012).
26. Valov, I. Interfacial interactions and their impact on redox-based resistive switching memories (ReRAMs). *Semicond. Sci. Technol.* **32**, 093006 (2017).
27. Seungho Cho, Chao Yun, Stefan Tappertzhofen, Ahmed Kursumovic, Shinbuhm Lee, Ping Lu, Quanxi Jia, Meng Fan, Jie Jian, Haiyan Wang, Stephan Hofmann & Judith L. MacManus-Driscoll. Self-assembled oxide films with tailored nanoscale ionic and electronic channels for controlled resistive switching | Nature Communications. *Nat. Commun.* **7**, 12373 (2016).
28. Baumberg, J. J., Aizpurua, J., Mikkelsen, M. H. & Smith, D. R. Extreme nanophotonics from ultrathin metallic gaps. *Nat. Mater.* **18**, 668–678 (2019).
29. Ranjan, A. *et al.* Analysis of quantum conductance, read disturb and switching statistics in HfO₂ RRAM using conductive AFM. *Microelectron. Reliab.* **64**, 172–178 (2016).

30. Aravind, P. K. & Metiu, H. The effects of the interaction between resonances in the electromagnetic response of a sphere-plane structure; applications to surface enhanced spectroscopy. *Surf. Sci.* **124**, 506–528 (1983).
31. P. Nordlander, E Prodan. Plasmon Hybridization in Nanoparticles near Metallic Surfaces. *Nano Lett.* **4**, 2209 (4).
32. Xiaojuan Lian, Xavier Cartoixà, Enrique Miranda, Luca Perniola, Riccardo Rurali, Shibing Long, Ming Liu, and Jordi Suñé. Multi-scale quantum point contact model for filamentary conduction in resistive random access memories devices. *J. Appl. Phys.* **115**, 244507 (2014).
33. Long, S. *et al.* Quantum-size effects in hafnium-oxide resistive switching. *Appl. Phys. Lett.* **102**, 183505 (2013).
34. Cartoixà, X., Rurali, R. & Suñé, J. Transport properties of oxygen vacancy filaments in metal/crystalline or amorphous HfO_2 /metal structures. *Phys. Rev. B* **86**, 165445 (2012).
35. Mertens, J. *et al.* Tracking Optical Welding through Groove Modes in Plasmonic Nanocavities. *Nano Lett.* **16**, 5605–5611 (2016).
36. Mertens, J. *et al.* Controlling Subnanometer Gaps in Plasmonic Dimers Using Graphene. *Nano Lett.* **13**, 5033–5038 (2013).
37. Tserkezis, C. *et al.* Hybridization of plasmonic antenna and cavity modes: Extreme optics of nanoparticle-on-mirror nanogaps. *Phys. Rev. A* **92**, 053811 (2015).
38. Demetriadou, A. *et al.* Spatiotemporal Dynamics and Control of Strong Coupling in Plasmonic Nanocavities. *ACS Photonics* **4**, 2410–2418 (2017).
39. Pflüger, J. & Fink, J. Chapter 13 - Determination of Optical Constants by High-Energy, Electron-Energy-Loss Spectroscopy (EELS). in *Handbook of Optical Constants of Solids* (ed. Palik, E. D.) 293–311 (Academic Press, 1997). doi:10.1016/B978-012544415-6.50055-8.
40. Pflüger, J., Fink, J., Weber, W., Bohnen, K. P. & Creelius, G. Dielectric properties of TiCx , TiNx , VCx , and VNx from 1.5 to 40 eV determined by electron-energy-loss spectroscopy. *Phys. Rev. B* **30**, 1155–1163 (1984).

41. Kos, D. *et al.* Electrically Controlled Nano and Micro Actuation in Memristive Switching Devices with On-Chip Gas Encapsulation. *Small* **14**, 1801599 (2018).
42. Li, Y. *et al.* Nanoscale Chemical and Valence Evolution at the Metal/Oxide Interface: A Case Study of Ti/SrTiO₃. *Adv. Mater. Interfaces* **3**, 1600201 (2016).
43. Stewart J. Clark, Matthew D. Segall, Chris J. Pickard, Phil J. Hasnip, Matt I. J. Probert, Keith Refson, Mike C. Payne. First principles methods using CASTEP. *Z. Für Krist. - Cryst. Mater.* (2005) doi:10.1524/zkri.220.5.567.65075.
44. Andrew J. Morris, Rebecca J. Nicholls, Chris J. Pickard, Jonathan R. Yates. OptaDOS: A tool for obtaining density of states, core-level and optical spectra from electronic structure codes - ScienceDirect. *Comput. Phys. Commun.* **185**, 1477–1485 (2014).
45. Accurately Simulate Photonic Components and Circuits. *Lumerical*
<https://www.lumerical.com/products/>.